Focused on IGF26 - 26th International Conference on Fracture and Structural Integrity

Visual Abstract

Effect of petrographic composition and chemistry of aggregate on the local and general fracture response of cementitious composites

M. Vyhlídal, I. Rozsypalová, H. Šimonová, B. Kucharczyková, P. Rovnaníková, Z. Keršner
Brno University of Technology, Faculty of Civil Engineering, Veveří 331/95, 602 00 Brno, Czech Republic
Michal.Vyhlidal@vutbr.cz, https://orcid.org/0000-0002-8035-6781
rozsypalova.i@fce.vutbr.cz, http://orcid.org/0000-0003-3109-3820
simonova.h@vutbr.cz, http://orcid.org/0000-0003-1537-6388
barbara.kucharczykova@vutbr.cz, http://orcid.org/0000-0002-7123-5099
rovnanikova.p@fce.vutbr.cz, http://orcid.org/0000-0002-6732-788X
kersner.z@fce.vutbr.cz, http://orcid.org/0000-0003-4724-6166

L. Vavro, M. Vavro
Czech Academy of Sciences, Institute of Geonics, Studentská 1768, 708 00 Ostrava-Poruba, Czech Republic
leona.vavro@ugn.cas.cz, http://orcid.org/0000-0002-4830-8691
martin.vavro@ugn.cas.cz, http://orcid.org/0000-0003-1446-460X

J. Němeček
Czech Technical University in Prague, Faculty of Civil Engineering, Department of Mechanics, Thákurova 7, 166 29 Prague, Czech Republic
jiri.nemecek@fsv.cvut.cz, http://orcid.org/0000-0002-3565-8182

ABSTRACT. This paper concerns the results of research into the influence of the composition of rock inclusions on the fracture response of cement-based composite specimens. Specially designed specimens of the nominal dimensions 40 × 40 × 160 mm with inclusions in the shape of prisms with nominal dimensions of 8 × 8 × 40 mm were provided with an initial central edge notch with a depth of 12 mm. These specimens, which were made of fine-grained cement-based composite with different types of rock inclusion – amphibolite, basalt, granite, and marble – were tested in the three-point bending configuration. Fracture surfaces were examined via scanning electron microscopy and local response in the vicinity of rock inclusions was characterized via the nanoindentation technique. The aim of this paper is to analyse the influence of the chemical/petrographic composition of rock inclusions on the effective mechanical fracture parameters of cement-based composites, as well as on the microstructural mechanical parameters of the interfacial transition zone. The results of this research indicate the significant dependence of the effective fracture parameters on the petrographic and related chemical composition of the rock inclusions.

Citation: Vyhlídal, M., Rozsypalová, I., Šimonová, H., Kucharczyková, B., Vavro, L., Vavro, M., Němeček, J., Rovnaníková, P., Keršner, Z. Influence of rock inclusion composition on the fracture response of cement-based composite specimens, Frattura ed Integrità Strutturale, 60 (2022) 13-29.

Received: 30.10.2021
Accepted: 17.01.2022
Online first: 22.01.2022
Published: 01.04.2022

KEYWORDS. Cement-based composite; Force–displacement diagram; Fracture test; Inclusion; Mechanical fracture parameters; Rocks.

INTRODUCTION

Cement-based composites, with concrete being the main representative of such composites, are widely used building materials. Concrete structures such as highway bridges, tunnels, dams, etc. are important parts of the infrastructure which should serve for many generations after their construction. In many cases, such structures show nonlinear, or more precisely, quasi-brittle behaviour – the ability to carry load continues even after the deviation from the linear branch of the force–displacement diagram until the peak point, after which a decrease in loading force follows until failure occurs, which is a phenomenon known as tensile softening [1]. The reason for this behaviour is, apart from strong heterogeneity, the existence of internal defects (pores, cracks, transition zones, etc.) or material discontinuities (e.g. inclusions), which work as obstacles to or promoters of crack propagation. Nevertheless, these discontinuities, which form stress concentrators that serve as potential weak elements in composites, are not given any consideration at all in the standards, e.g. [2].
In this paper, material discontinuities are formed by rock inclusions placed in the middle of the test specimens. These specimens made of fine-grained cement-based composite with different types of rock inclusion – amphibolite, basalt, granite, and marble – were tested in the three-point bending configuration. The rock inclusions were made using a saw with a diamond blade. After the tests, the fracture surfaces were examined via scanning electron microscopy (SEM) and local response in the vicinity of the rock inclusions was characterized via the nanoindentation technique [3]. Assuming that the test specimens were manufactured, compacted and tested in the same way and that the inclusions' surfaces had the same roughness, the only way to explain the deviation in overall fracture response should be, according to [4] and [5], chemical adhesion. The aim of this paper is to identify the influence of mineralogical composition of rock inclusions on the overall fracture response of the above-described cement-based composite specimens.

THEORETICAL BACKGROUND

Interface shear transfer

The bond mechanism is the interaction between reinforcement and concrete. The components of bond resistance are a combination of different mechanisms – chemical adhesion, friction, mechanical interlocking and the dowel action of reinforcement crossing the interface [4].
The dowel action of reinforcement crossing the interface is the result of the lateral displacement of the upper and lower reinforcement ends due to shear slip along the interface. The transfer of shear forces along the interface is thus provided by the bending, shear and axial stresses in reinforcement bars caused by this lateral displacement [4].
The mechanical interlocking resistance is the result of the forces acting perpendicular to the ribs of reinforcement. This resistance takes place in the case of excessive and irregular roughness when keying and undercutting effects occur. This effect will only take place if the aggregates/ribs protrude sufficiently from the surface [4].
The frictional resistance is the result of the compression forces perpendicular to the interface and also depends on the degree of interface roughness. In [5], there is a recommendation for the values of the coefficient of friction μ for a constant confining stress σ_c depending on whether the interface is smooth, rough or very rough. Several parameters are also described for the classification of the concrete surface roughness, such as mean roughness R_a and the mean peak-to-valley height R_z.
Although adhesive shear resistance is in the range of lower units of MPa for concrete grades ≤ C50/60, adhesive bonding can significantly affect overall shear resistance [4]. Adhesive resistance is a result of chemical and physical bonding due to van der Waals forces. For this effect to occur, the related slip at failure must be very small, otherwise the effect will vanish. Adhesive resistance strongly depends on the real surface of the contact area, and the quality, composition and properties (e.g. porosity) of concrete [4]. It is connected to the formation of the interfacial transition zone – see the next section – at the aggregate–matrix or reinforcement–matrix interface, which is regarded as the weakest element of cement-based composites.

The Interfacial Transition Zone

The existence of the Interfacial Transition Zone (ITZ) between aggregate and cement paste was first described in the 1950s by Farran [6]. The ITZ is a region of about 50 μm in size, and its significant feature is mainly its higher porosity compared to the bulk matrix [7]. The microstructure of the region is formed mainly by ettringite needles and portlandite plates, while

the amount of unhydrated cement grains is reduced [8]. The local increase in porosity is in a good agreement with the lower values displayed by the mechanical fracture parameters of the ITZ, see e.g. [3]. These lower values are inevitably connected with the bond resistance.

EXPERIMENTAL PART

Rocks

Four basic types of rocks were selected for the preparation of rock inclusions. Specifically, these were: (i) amphibolite from the former Rožná I uranium mine, (ii) olivine basalt from the Bílčice quarry, (iii) biotite granite from the Černá Voda-Nový lom quarry, and (iv) marble from the Horní Lipová-Mramorový vrch quarry (Fig. 1). These rocks were chosen deliberately, as they essentially represent the main raw materials used in the production of crushed aggregates in the Czech Republic. More than 200 deposits of crushed stone are currently quarried on the territory of the Czech Republic [9], of which about 23 % are granite deposits, approx. 12 % basalt deposits, around 7 % amphibolite deposits and approx. 2 % marbles. In terms of the total production of crushed aggregates in the Czech Republic, basaltic volcanites account for about 25 % and acidic plutonites such as granites about 20 % of the currently produced aggregates [9].

Figure 1: Rock specimens used for inclusion preparation after fracture tests (in order from left to right): amphibolite, basalt, granite and marble.

Dark grey to black, coarse-grained amphibolite from the Rožná I mine (approximately 40 km NW from Brno) is mostly formed from amphibole (approx. 60–70 % of the rock volume), which varies in composition from tschermakite to magnesiohornblende [10]. Other rock components consist of plagioclase, the basicity of which corresponds to andesine up to labradorite (approx. 20–30 vol. %) and rarely occurring quartz (up to 10 vol. %). Typical accessory minerals are represented by titanite, zircon and opaque phases, probably pyrite. The rock exhibits plane parallel structure and granonematoblastic texture.

Olivine basalt from the Bílčice quarry (approx. 40 km NE from Olomouc) typically exhibits massive to vesicular structure and porphyritic texture, with pilotaxitic texture of the rock matrix. Phenocrysts are predominantly formed by olivine (approx. 15–20 %), while other rock forming minerals are represented by pyroxene (in particular augite, approx. 37–45 %), calcium-rich plagioclase of labradorite composition (about 20–30 %) and magnetite (up to 20 %). The proportion of amorphous phase (basaltic glass) is up to 3 %. In addition to aggregate production, this basalt was also used in the past for mineral wool manufacturing [11].

The "light Silesian granite" from the Černá Voda-Nový lom quarry (approx. 10 km N from the city of Jeseník) is petrographically represented by light grey to grey, medium-grained biotite granite, which typically features holocrystalline, equigranular, hypautomorphic to panxenomorphic granitic texture and massive structure. Its mineral composition is relatively simple, with felsic rock components formed by quartz (approx. 30 %), K-feldspars (approx. 40 %) and plagioclase (approx. 25 %), while biotite (approx. 5 %) is the basic mafic mineral. Accessory minerals include zircon, titanite, apatite, magnetite and rare allanite [12].

The marble quarried at the Horní Lipová-Mramorový vrch deposit (approx. 7 km W from the city of Jeseník) is a well-known building and decorative stone material often referred to as "dark Lipová marble". The rock typically has a light grey to dark grey colour, often with well-visible banding. It is almost entirely (often more than 90 %) composed of calcite, other

minerals such as graphite, quartz, muscovite, and pyrite rarely occur, some of them even only as accessories. The rock exhibits massive to plane parallel structure and granoblastic texture.
Microscopic views of the rocks used for inclusion preparation are shown in Fig. 2.

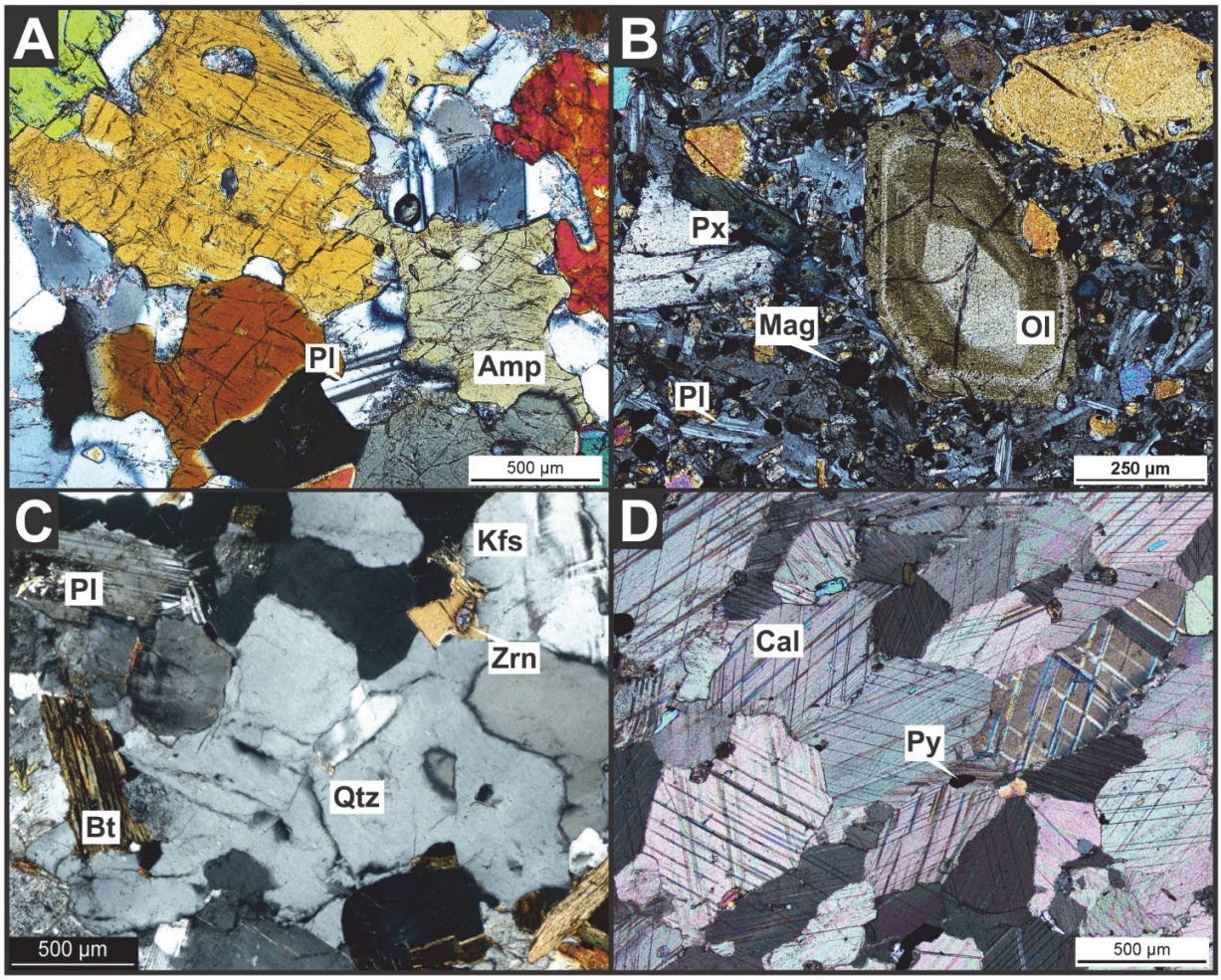

Figure 2: Micrographs of the studied rocks (polished thin sections, transmitted light, crossed polarizers). A – amphibolite, B – basalt, C – granite, D – marble. Rock-forming mineral abbreviations (in alphabetical order): Amp – amphibole, Bt – biotite, Cal – calcite, Kfs – K-feldspar, Mag – magnetite, Ol – olivine, Pl – plagioclase, Px – pyroxene, Py – pyrite, Qtz – quartz, Zrn – zircon.

The chemical composition of the rocks used for inclusion preparation was determined semiquantitatively using a XEPOS X-ray fluorescence (XRF) energy dispersive spectrometer (Spectro Analytical Instruments GmbH, Germany). The milled rock sample was mixed with wax and a tablet was moulded and then analysed in a protective atmosphere (He). The results of determining the chemical compositions of the rocks are shown in Tab. 1.

Inclusion	SiO_2	TiO_2	Al_2O_3	Fe_2O_3*	MnO	MgO	CaO	Na_2O	K_2O	P_2O_5	LOI	Σ
Amphibolite	44.80	0.88	15.25	12.08	0.22	9.56	12.47	1.57	1.05	0.05	1.57	99.50
Basalt	42.21	2.66	13.36	13.72	0.22	8.26	12.90	3.80	0.76	0.97	0.56	99.42
Granite	71.60	0.29	13.70	2.68	0.04	0.41	1.95	3.45	5.02	0.11	0.43	99.68
Marble	2.31	0.12	1.12	0.72	0.01	0.70	53.10	0.19	0.21	0.06	41.31	99.85

Explanations: * = iron in the form of Fe_2O_3, LOI = loss-on-ignition; the samples were burned in a muffle furnace for 3 hours at 1100°C

Table 1: Chemical composition of rock inclusions determined using XRF spectrometry [%].

Physicomechanical properties and fracture tests of rocks

The tested rocks were acquired in the form of blocks of irregular shape and with a side length of about 0.3–0.4 m. Cylindrical samples measuring 48 mm in diameter were subsequently drilled from the blocks under laboratory conditions. The ends of the drill cores were finally cut perpendicularly to their length, so that the *L*:*D* ratio (length-to-diameter ratio or slenderness ratio) of the prepared test specimens was about 2. Basic physical and mechanical characteristics were tested on dry specimens according to standard procedures represented by relevant European standards [13, 14] and suggested testing methods of the International Society for Rock Mechanics [15-1716]. The mechanical properties of the studied rocks were determined by computer-controlled mechanical presses: the FPZ 100 (VEB TIW Rauenstein Thüringer, Germany) and the ZWICK 1494 (Zwick/Roell, Germany).

In order to determine the fracture toughness and other important mechanical fracture properties of the input rocks, the three-point bending test was performed. For this test, long cylindrical specimens with a chevron (V-shaped) notch perpendicular to the specimen axis were used. A clip-on gauge type of extensometer was attached at the mouth of each chevron notch, allowing the relative crack face opening (*CMOD* – crack mouth opening displacement) to be measured. Cylindrical test specimens of 48 mm in diameter and about 190 mm in length were drilled from the rock blocks. A diamond blade was used to cut the chevron notches with an internal angle of 90° and a thickness of 1.5 mm perpendicular to the core body axis and positioned in the centre of each sample. After the chevron notches had been cut, the test specimens were dried to a constant weight. Fracture toughness was calculated from measured force *F* vs. *CMOD* diagrams obtained from a three-point bending test which was carried out at room temperature on an FPZ 100 power press with displacement control at a constant loading rate of 0.1 mm·min^{-1}. For more details about the methods employed in this test, see [18] or [19].

The inclusions were made using a saw with a diamond blade to cut them from all above-mentioned rock types – amphibolite, basalt, granite, and marble.

Matrix material

The matrix of the test specimens was prepared from a fine-grained cement-based composite. The fresh mixture consisted of CEM I 42.5 R Portland cement (Mokrá cement plant, Czech Republic), EN 196-1 standard quartz sand with a maximum grain size of 2 mm, and water in the ratio 1:3:0.35 (cement:sand:water). To ensure workability, a polycarboxylate-based high-range water-reducing admixture (Sika SVC 4035) was added in an amount of 1 % by cement mass. For more details, see [20].

Specimens

The specimens with nominal dimensions of 40 × 40 × 160 mm containing an internal inclusion with nominal dimensions of 8 × 8 × 40 mm placed in the middle of the span above the initial notch were manufactured for the fracture tests, see Fig. 3. The only difference between the test sets was the type of rock inclusion – amphibolite, basalt, granite, or marble. Each test set contained three test specimens. A total amount of 15 specimens were tested – 3 reference specimens (without inclusion), 3 specimens with amphibolite inclusion, 3 specimens with basalt inclusion, 3 specimens with granite inclusion, and 3 specimens with marble inclusion.

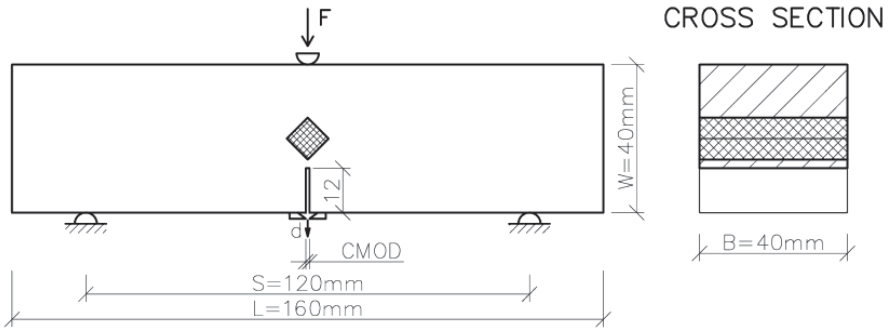

Figure 3: Specimen geometry and fracture test configuration [20].

Three-part polyethylene (PE) moulds were used to produce the test specimens. The rock inclusions were fixed in position in each part of the moulds before they were filled, see Fig. 4. The mixture was prepared under laboratory conditions using a hand-held paddle mixer. After pouring and compaction of the fresh mixture, the moulds were covered with a thin PE foil and stored under stable laboratory conditions with a temperature of (22 ± 2) °C for 3 days. After demoulding, the test

specimens were cured in a water bath until they were tested. The initial notch was made just before the fracture tests using a saw with a diamond blade, the notch depth being approximately 1/3 of specimen depth.

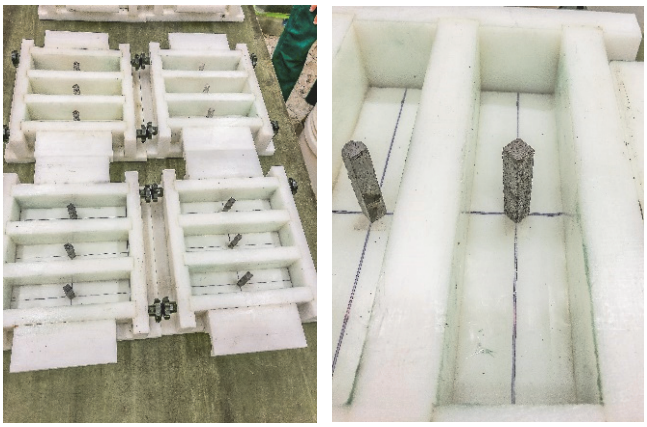

Figure 4: Moulds defining the final shape of the specimens with fixed rock inclusions.

Fracture tests of test specimens

To determine the influence of the ITZ on the fracture behaviour of fine-grained cement-based composite, fracture tests were conducted on the aforementioned specially designed specimens via three-point bending. The experiments were conducted using a very stiff LabTest 6-1000 multi-purpose mechanical testing machine (LaborTech Ltd., Czech Republic) with a load range of 0−1000 kN. The fracture tests were conducted under monotonic loading conditions with a constant displacement increment of 0.02 mm·min^{-1}. The load span was 120 mm.

During the experiment, besides the force (F), vertical mid-span displacement (d) and *CMOD* were continuously recorded. In order to measure *CMOD*, a strain gauge was fixed between steel blades, which were placed in close proximity to the notch. The mid-span displacement was measured using inductive sensors. As a result, both $F-d$ and $F-CMOD$ diagrams were obtained. An illustration of the three-point bending fracture test configuration is shown in Fig. 5.

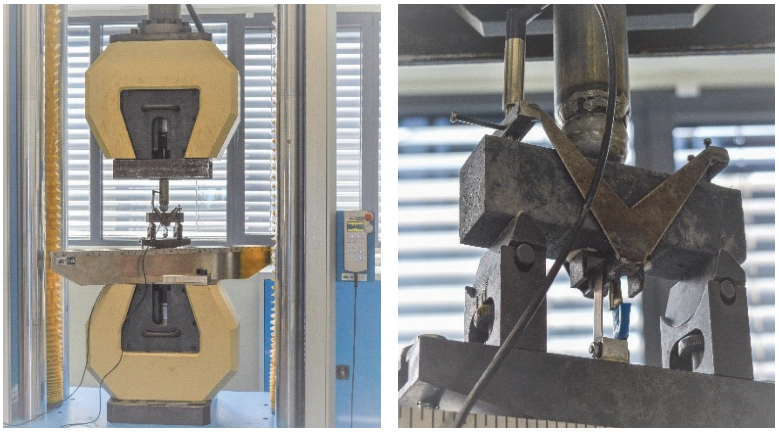

Figure 5: Three-point bending fracture test – LabTest testing machine (on the left); detail of measuring equipment (on the right).

Scanning electron microscopy measurements

After the fracture tests, the resulting fracture surfaces were examined via scanning electron microscopy at the AdMaS science centre, which is part of The Faculty of Civil Engineering at Brno University of Technology, and at the Institute of Theoretical and Applied Mechanics (ITAM) of the Czech Academy of Sciences. A TESCAN MIRA3 XMU scanning electron microscope with an environmental probe with 3D imaging was used.

In this paper, micrographs created by the detection of secondary electrons (SE) and backscattered electrons (BSE) are presented. SE are created by inelastic scattering of the beam electrons, while BSE are created by elastic scattering and are in fact primary electrons returning after a Coulomb interaction. SE thus provide information about topography, while BSE, in contrast, provides information about composition depending on atomic number Z [21].

Nanoindentation measurements

Nanoindentation was applied in the vicinity of each inclusion (ITZ zone) to reveal any changes in micromechanical response [22]. A Hysitron TriboLab TI-700 nanohardness tester equipped with a Berkovich diamond tip was used. A load-controlled test with the trapezoidal loading function (linear loading for 1 s, holding for 20 s and 1 s unloading) to a maximum force of 2 mN was prescribed for each indent. A rectangular matrix of about 100−200 indents was positioned partly to the inclusion, ITZ and bulk material. The matrix contained several rows with an inter-indent separation of 2−3 μm. Young's modulus E and hardness H were estimated by [23] theory (assuming Poisson's ratio ν = 0.2) as

$$H = \frac{F}{A_c} \tag{1}$$

$$E = \frac{1}{1-\nu^2}\frac{S\sqrt{\pi}}{2\beta\sqrt{A_c}} \tag{2}$$

where F is the maximum indentation force, S and A_c are the contact stiffness and area, respectively, and β is the tip correction factor. During the holding period, time-dependent deformation is characterized with the creep indentation parameter, the *CIT*, as

$$CIT_{(P,t_1,t_2)} = \frac{h_2 - h_1}{h_1} \times 100 \tag{3}$$

which is defined as a relative change between indentation depths h_1 encountered at time t_1 and h_2 at time t_2, respectively (i. e. the *CIT* depends on the contact force F and the time of holding period). Creep was also described with the creep compliance function assuming step loading as:

$$J(t) = \frac{2h^2(t)}{\pi\left(1-\nu^2\right)F\tan\alpha} \tag{4}$$

where $h(t)$ is the depth of the indent at time t, F is the loading force and a is the angle between the surface and edge of the tip (for a Berkovich diamond tip a = 19.7°). Although the assumption of step loading is not perfectly fulfilled, Eq. 4 gives a good estimate for the $J(t)$.

RESULTS

In this section, the results of fracture tests, nanoindentation measurements and SEM measurements are presented.

Physico-mechanical properties and fracture tests of rocks

Before fracture testing, some fundamental physical and mechanical rock properties were determined since these were assumed to influence the fracture mechanical behaviour of the studied rocks. Specifically, bulk density ρ, ultrasonic wave velocity v_P, water absorption capacity under atmospheric pressure w_{atm}, total porosity φ, and uniaxial compressive strength σ_c were determined on cylindrical specimens with an *L*:*D* ratio of 2 (48 mm in diameter, 96 mm high). Tensile splitting strength σ_t, determined by the Brazilian test, was measured on disc-like specimens with an *L*:*D* ratio of 0.7 (48 mm in diameter, 34 mm thick). Obtained results which represent the average value calculated from at least five individual measurements are shown in Tab. 2.

As stated in previous text, for the purpose of estimating fracture behaviour, the chevron bend (CB) test was performed and the mode I fracture toughness and other important mechanical fracture properties of the selected rocks were evaluated (see Tab. 3). Here, E_{agg} is the bending Young's modulus, ν_{agg} represents Poisson's ratio, $K_{Ic,\,agg}$ is the mode I stress intensity factor (fracture toughness), $G_{Ic,\,agg}$ is the mode I critical strain energy release rate, and $G_{F,\,agg}$ represents fracture energy.

Inclusion material	ρ [kg·m^{-3}]	v_P [km·s^{-1}]	w_{atm} [%]	φ [%]	σ_c [MPa]	σ_t [MPa]
Amphibolite	2990	6.68	0.13	0.81	193	13.5
Basalt	2970	5.49	1.16	3.44	232	12.3
Granite	2620	4.80	0.31	1.50	185	7.5
Marble	2710	4.92	0.17	0.69	107	8.9

Table 2: Physical and mechanical properties of rocks.

Inclusion material	E_{agg} [GPa]	ν_{agg} [–]	$K_{Ic,\,agg}$ [MPa·m$^{1/2}$]	$G_{Ic,\,agg}$ [J·m^{-2}]	$G_{F,\,agg}$ [J·m^{-2}]
Amphibolite	143.0	0.16	3.37	79.6	448.0
Basalt	87.8	0.15	2.25	57.4	339.0
Granite	59.6	0.18	1.26	26.7	189.4
Marble	108.1	0.20	1.85	31.6	249.2

Table 3: Mechanical fracture properties of rocks.

Fracture tests of specimens

Typical development of F depending on the value of d for specimens with rock inclusion (solid line) and specimens made only from matrix (dashed line) can be seen in Fig. 6. Although matrix was "reinforced" by rock inclusions, the reduction of maximum force values is apparent. The ascending branch is almost linear for all specimens while the descending branch differs especially in the case of amphibolite and granite inclusion. In these cases, descending branch contains local peaks, which are not typical for quasi-brittle behaviour of cement-based composites. These local peaks relate to specific crack propagation direction and occur when the crack changed the propagation direction at the edge of the inclusion; for more details see [24].

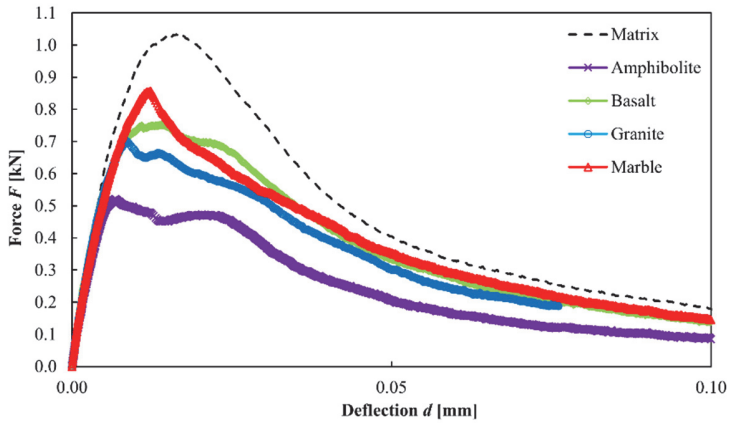

Figure 6: Selected F–d diagram for specimens with rock inclusion/reference specimens consisting of matrix only (dashed line).

During the fracture tests, all possible crack propagation directions were observed, see Fig. 7. The crack propagation paths labelled a) and b) in Fig. 7 were observed only for the one specimen with a marble inclusion, while for the rest of the specimens with a marble inclusion, as well as for those with basalt inclusions, crack propagation path c) was observed. In the case of specimens with amphibolite or granite inclusion, the d) crack propagation path occurred. It is evident, that the crack propagation paths in the case a) and b) are caused by low hardness (3 on Mohs scale) and especially by perfect cleavage of calcite as a dominant rock-forming mineral of marble. Crack propagation path c) indicates a high degree

of cohesion between rock inclusion and cement matrix and in the case of basalt it is probably due to the vesicular texture, i. e. the presence of pores on the surface of the inclusion. The pores increase the real surface of the contact area between cement matrix and aggregate inclusion which probably contributes to adhesive resistance improvement. Case d), found for amphibolite and granite, is then unfortunately probably due to the method of preparation of inclusions. Because of being sawn using a diamond blade, the inclusions have flat and smooth surfaces, which causes them to have lower cohesion with the cement matrix than there probably should be, see [24]. Therefore, in the event of a future continuation of these experiments, it will be appropriate to consider another method of preparing the inclusions, for example by means of water jet cutting.

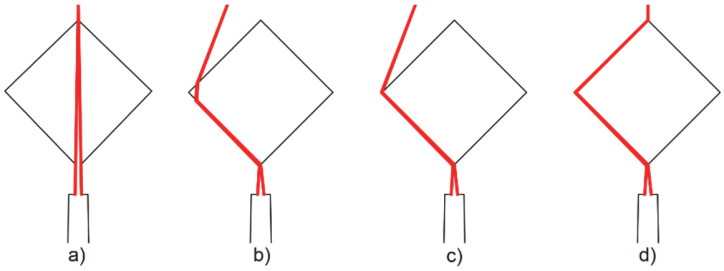

Figure 7: Illustration of crack propagation paths.

Specimens after fracture testing can be seen with their crack propagation paths in Fig. 8. Please note that the specimens are labelled with the first three initial letters of the material from which the inclusions are made (e. g. AMP for amphibolite, BAS for basalt etc.). The specimens in the right side of Fig. 8 are reference specimens which were made only from fine-grained cement-based material (matrix) for the determination of the mechanical fracture properties of the matrix.

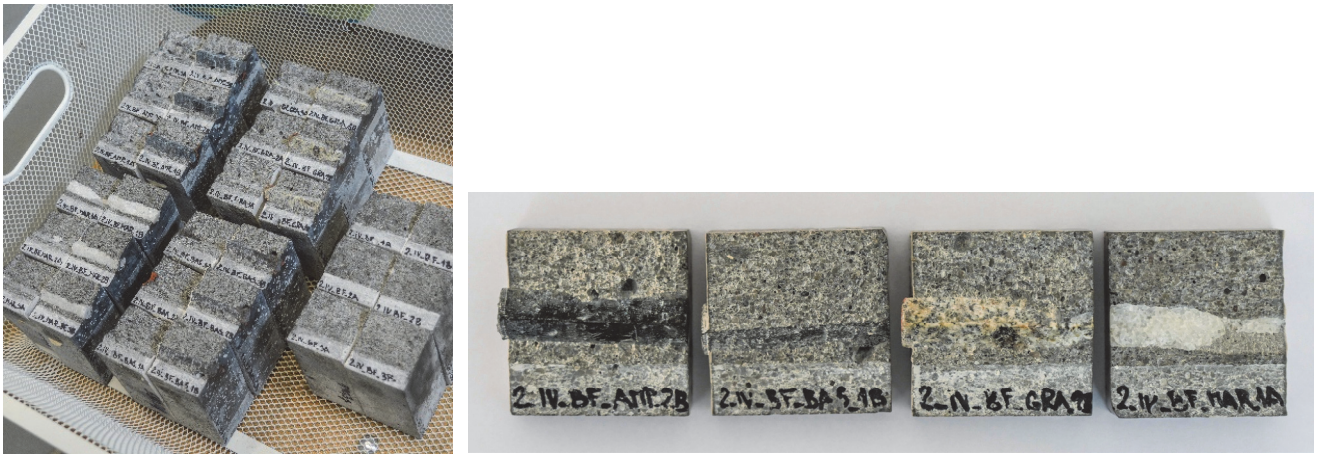

Figure 8: Specimens after fracture testing (left), and selected details with inclusions: amphibolite, basalt, granite, marble.

The measured F–d diagrams were used to estimate values for the maximal force F_{max}, Young's modulus of elasticity E, specific fracture energy G_F, fracture toughness K_{Ic} and effective fracture toughness $K_{Ic,e}$.
Young's modulus of elasticity E was estimated from the first, almost linear part of these diagrams, see [1], as:

$$E = \frac{F_i}{4Bd_i}\left(\frac{S}{W}\right)^3\left[1+\frac{5qS}{8F_i}+\left(\frac{W}{S}\right)^2 2.70+1.35\frac{qS}{F_i}-0.84\left(\frac{W}{S}\right)^3\right]+\frac{9}{2}\frac{F_i}{Bd_i}\left(1+\frac{qS}{2F_i}\right)\left(\frac{S}{W}\right)^2 F_1(\alpha_0) \qquad (5)$$

where F_i, d_i is force in kN, respectively deflection in mm read from the linear part of F–d diagrams. S, B and W are dimensions of the specimen in mm, q is self-weigh of the specimen in kN/m and $F_1(a_0)$ is shape function. First term of equation is calculated from the deflection of the whole cross-section (without crack) caused not only from the bending moment but also from the shear force. The second term includes the effect of the notch depth and is based on the Castigliano principles,

see [1] for more details. Specific fracture energy G_F represents the energy necessary for the creation of a unit area of a crack and was calculated using the work-of-fracture method [25] as:

$$G_F = \frac{W_F}{A_{lig}} \tag{6}$$

where G_F is specific fracture energy in J·m^{-2}, A_{lig} is area of ligament and W_F is work of fracture in N·m.
Fracture toughness K_{Ic} represents a linear elastic brittle material's resistance to crack propagation and was estimated from F_{max} according to [1] as:

$$K_{Ic} = \frac{6F_{max}S}{4BW^2}\sqrt{a}Y(\alpha) \tag{7}$$

where F_{max} represents peak load in kN, a is crack length in mm and Y *(a)* is shape function.
In contrast to K_{Ic}, the effective fracture toughness $K_{Ic,e}$ was determined based on the Effective Crack Model [1], in which the difference between the initial tangent stiffness and the secant stiffness of the specimen at peak load F_{max} is considered. The effective crack length ae is obtained by extending the initial crack length a_0 to such a value that the maximal deflection d_{max} will be achieved by applying the peak load F_{max} with constant value of Young's modulus of elasticity E.
Mean values and standard deviations of the determined mechanical fracture parameters can be seen in Tab. 4.

Inclusion material	F_{max} [kN]	E [GPa]	G_F [J·m^{-2}]	K_{Ic} [MPa·m$^{1/2}$]	$K_{Ic,e}$ [MPa·m$^{1/2}$]
Amphibolite	0.529±0.057	39.7±1.69	30.48±4.78	0.295±0.033	0.385±0.028
Basalt	0.791±0.076	42.1±1.94	41.99±6.30	0.443±0.043	0.720±0.089
Granite	0.829±0.142	46.5±4.48	42.35±4.61	0.462±0.081	0.625±0.184
Marble	0.828±0.054	39.8±2.65	57.73±4.97	0.462±0.031	0.910±0.252

Table 4: Mechanical fracture parameters (mean values from 3 measurements) [20].

Inclusion material	$E_{mic,20}$ [GPa]	$E_{mic,50}$ [GPa]	H_{50} [GPa]	$J_{50}(t)$ [GPa^{-1}]
Amphibolite	23.2	25.8	0.75	0.188
Basalt	32.8	36.1	1.32	0.053
Granite	34.2	37.9	2.12	0.045
Marble	34.4	34.5	1.33	0.063

Table 5: Results of nanoindentation measurements [3].

Nanoindentation measurements

The results for E_{mic}, H, *CIT* and $J(t)$ were evaluated with regard to their dependence on distance from an inclusion. E_{mic}, H exhibit a gradual increase with distance, defining a weaker ITZ around the rock inclusion in the region of 0–20 μm. The region is characterized by a lower modulus and a lower hardness compared to the bulk for all specimens, as already detected in [3], see Tab. 5. Slightly lower E_{mic} and H values among the specimens can be found for specimens with amphibolite inclusions. The *CIT* parameter in the ITZ around inclusions is always higher due to the higher creep encountered in this zone. The highest amount of creep and the highest *CIT* and $J(t)$ are exhibited by the specimens with amphibolite inclusions, especially in the ITZ of these specimens. Microstructurally, the ITZ can be described as having a higher porosity around the aggregate [7]. Consistently, the evolution of Young's modulus and hardness has a negative correlation with porosity, while *CIT* and the amount of creep scales with porosity.
To quantify the influence of micromechanical parameters measured by nanoindentation, the mean hardness (H_{50}) and average creep compliance $J_{50}(t)$ values were calculated over an ITZ region of 50 μm, while the mean Young's modulus

values were calculated over ITZ regions of 20 μm ($E_{mic,20}$) and 50 μm ($E_{mic,50}$) due to the higher values of porosity in the first 20 μm of the ITZ; see [26] or [27].

Microstructure of the ITZ

In the following four figures (Figs. 9–12), the micrographs on the left display the hardened cement that adhered to the inclusions after the mechanical tests; the microstructures of the specimens with amphibolite, basalt and granite are very similar in character. The specimens with marble inclusions are different; there are large portlandite crystals in many places, and the CSH and CAH phases have a less porous structure.

The middle micrographs show the connection between the hardened cement and the surfaces of the inclusions. No connection was found between the cement and the surfaces for the specimens with amphibole, basalt and granite. However, hardened cement adheres to the surface of the marble inclusions and forms a close bond.

Given that the used inclusions do not contain components that tend to react with hardened cement, such as pozzolans, or form new phases in the ITZ, the adhesion probably results from the surface roughness of the inclusions. This property of the inclusions and the adhesion of the hardened cement to their surface have not yet been measured; they will be the subject of further research.

The third (right-hand) micrographs in the series below show the connection between the inclusion and the hardened cement in the polished samples. The images of the polished samples do not fully support the results obtained from the fracture surfaces of the specimens. Differences in the faces of the materials (i. e. hardened cement and inclusion) are evident but the join cannot be relevantly evaluated; the join was probably filled with grinding dust during the preparation of the sample. On the other hand, in the case of the specimen with marble a crack was formed between both materials.

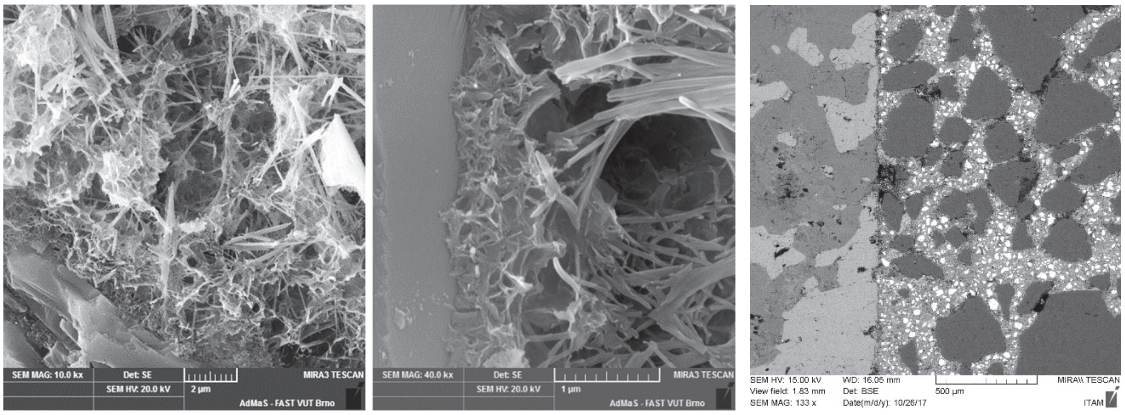

Figure 9: Microstructure of the amphibolite–matrix interface characterized by SEM via the detection of secondary electrons (on the left) and backscattered electrons. The first micrograph, which was captured by Dr. Bayer, has already been published in [24] to illustrate the interface microstructure.

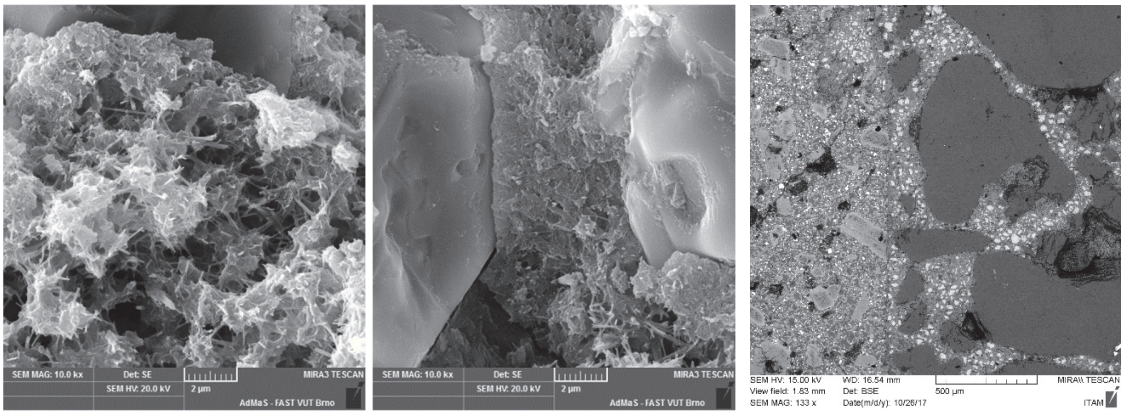

Figure 10: Microstructure of the basalt–matrix interface characterized by SEM via the detection of secondary electrons (on the left) and backscattered electrons.

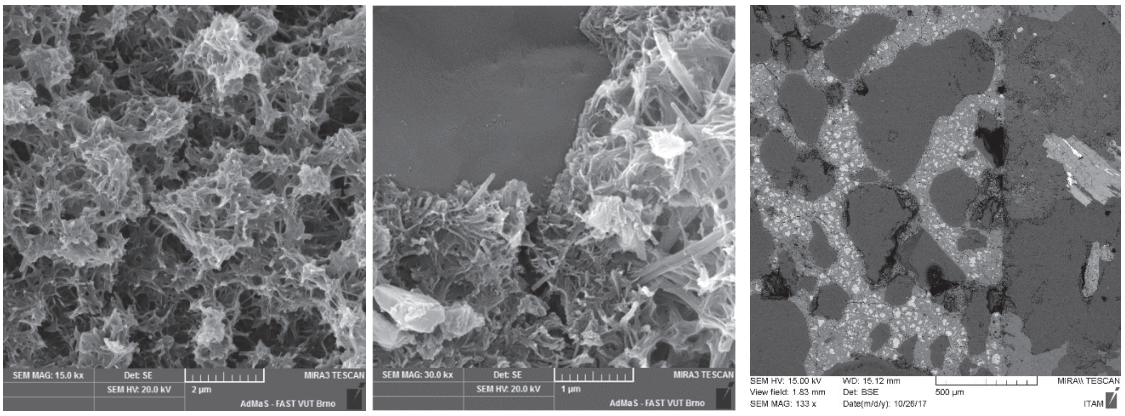

Figure 11: Microstructure of the granite–matrix interface characterized by SEM via the detection of secondary electrons (on the left) and backscattered electrons.

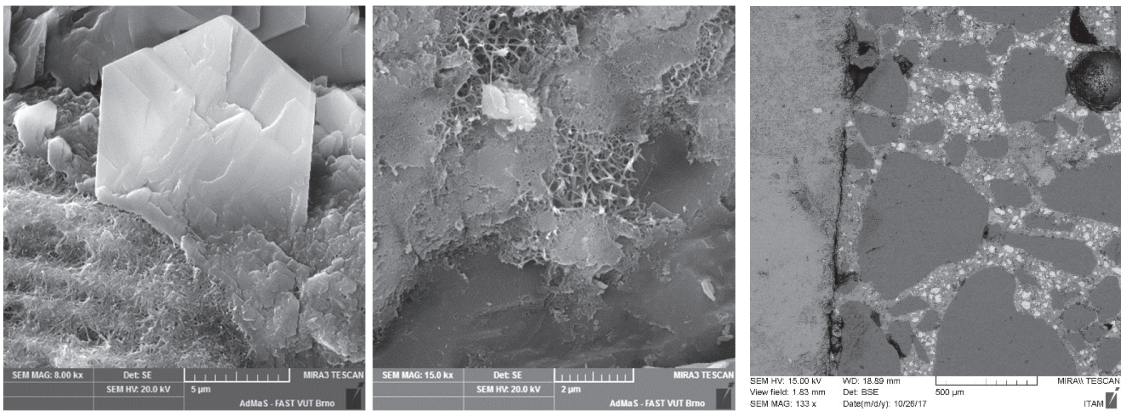

Figure 12: Microstructure of the marble–matrix interface characterized by SEM via the detection of secondary electrons (on the left) and backscattered electrons.

DISCUSSION

In this section, the correlations between components will be described and discussed. The Pearson's correlation coefficient r_{xy}, which is the covariance S_{XY} of the two variables x and y divided by their standard deviation S_{XX}, S_{YY} respectively – see Eq. 8 [28], is applied to the data. In general, this correlation means a linear dependence between the variables x and y. The degree of correlation is expressed by a correlation coefficient, which can take values from −1 to +1.

$$r_{xy} = \frac{S_{XY}}{\sqrt{S_{XX} S_{YY}}} = \frac{\sum (x_i - \overline{x})(y_i - \overline{y})}{\sum (x_i - \overline{x})^2 (y_i - \overline{y})^2} \tag{8}$$

The correlations will be divided according to their correlation coefficient value (dimensionless) into five groups – 0.00–0.30 weak, 0.31–0.70 moderate, 0.71–0.80 strong, 0.81–0.99 very strong and 1 for perfect – according to [29], [30], [31]. Negative correlations can be obtained by changing the sign to negative.

Before making these detailed correlations, it should be emphasized that the mechanical fracture parameters of the rocks under study correspond very closely with their basic physical and mechanical properties. It is obvious that high bulk density, low porosity and corresponding high strength properties are reflected, for example, in high rock fracture toughness values. Regarding the correlation between the rock indirect tensile strength measured by the Brazilian test and the fracture toughness

of mode I, the obtained results can be expressed by the relationship $\sigma_t \approx 4.0$ to 6.0 K_{Ic}., which is in accordance with the results published in [18] and [32].

Influence of the chemical composition of rock on the overall mechanical fracture parameters of rock

The influence of the chemical composition of rock on the overall mechanical fracture parameters of rock is presented in Tab. 6. The correlation between the fracture toughness of rock $K_{Ic,agg}$ and the chemical composition is mainly weak or moderate. The correlation between the Poisson's ratio of a rock and its chemical composition is very strongly negative in the case of TiO_2, Al_2O_3, Fe_2O_3, MnO and MgO. The only one very strong positive correlation between E_{agg} and chemical composition was found for MgO. However, the deeper causes of chemical influence are still being researched, and thus only correlations are presented here.

	SiO_2	TiO_2	Al_2O_3	Fe_2O_3	MnO	MgO	CaO	Na_2O	K_2O	P_2O_5
$K_{Ic,\,agg}$	–0.47	–0.03	–0.05	0.38	0.45	0.60	0.32	–0.64	–0.70	–0.28
ν_{agg}	–0.48	**–0.85**	**–0.82**	**–0.96**	**–0.95**	**–0.88**	0.69	–0.66	0.09	–0.67
E_{agg}	–0.14	0.30	0.34	0.72	0.78	**0.87**	–0.06	–0.25	–0.58	0.00
$G_{Ic,\,agg}$	0.06	0.48	0.54	**0.87**	**0.91**	**0.96**	–0.28	0.01	–0.47	0.19
$G_{F,\,agg}$	–0.08	0.43	0.42	**0.81**	**0.86**	**0.94**	–0.14	–0.12	–0.57	0.15

Table 6: Influence of the chemical composition of rock on the overall mechanical fracture parameters of rock: coefficients of correlation.

Influence of the chemical composition of rock on micromechanical parameters measured by nanoindentation

The influence of the chemical composition of rock on micromechanical parameters measured by nanoindentation is presented in Tab. 7. There is weak negative correlation between Young's modulus E_{mic} and minerals, except in the case of Na_2O, K_2O and P_2O_5, where there is weak to moderate positive correlation. Moderate to strong negative correlation occurred in the case of MgO and MnO. As regards hardness, we obtained moderate positive correlation in the case of SiO_2 and Na_2O. A strong to very strong positive correlation was found in the case of K_2O. The correlation between minerals and average creep compliance $J_{50}(t)$ is mainly moderate to weak.

More than the mineralogical composition of the inclusion, the properties of the ITZ will be influenced by the mineralogy of the newly formed phases at the aggregate-matrix interface, which was unfortunately not monitored.

	SiO_2	TiO_2	Al_2O_3	Fe_2O_3	MnO	MgO	CaO	Na_2O	K_2O	P_2O_5
$E_{mic,20}$	–0.13	–0.08	–0.51	–0.60	–0.68	–0.76	0.28	0.18	0.25	0.24
$E_{mic,50}$	0.16	0.07	–0.23	–0.44	–0.53	–0.65	–0.02	0.46	0.44	0.36
H_{50}	0.46	–0.26	–0.03	–0.59	–0.64	–0.76	–0.26	0.47	**0.81**	–0.01
$J_{50}(t)$	0.00	–0.07	0.36	0.47	0.55	0.66	–0.12	–0.36	–0.31	–0.38

Table 7: Influence of the chemical composition of rock on micromechanical parameters measured by nanoindentation: coefficients of correlation.

Influence of the mechanical fracture properties of rock on micromechanical parameters measured by nanoindentation

The influence of the mechanical fracture properties of rock on micromechanical parameters is presented in Tab. 8. There is very strong negative correlation between the mechanical fracture parameters of rocks and micromechanical parameters, except for in the case average creep compliance $J_{50}(t)$, where there is a very strong positive correlation. The only exception is the Poisson's ratio ν_{agg}, which has a weak to moderate correlation with the mechanical fracture parameters of rocks.

	$K_{Ic,agg}$	ν_{agg}	E_{agg}	$G_{Ic,agg}$	$G_{F,agg}$
$E_{mic,20}$	**–0.81**	0.49	**–0.93**	**–0.90**	**–0.89**
$E_{mic,50}$	**–0.94**	0.27	**–0.93**	**–0.83**	**–0.87**
H_{50}	**–0.96**	0.36	**–0.94**	**–0.85**	**–0.92**
$J_{50}(t)$	**0.88**	–0.33	**0.91**	**0.84**	**0.85**

Table 8: Influence of the mechanical fracture properties of rock on micromechanical parameters measured by nanoindentation: coefficients of correlation.

Influence of the mechanical fracture properties of rock on the overall fracture behaviour of test specimens

The influence of the mechanical fracture properties of rock on the overall fracture behaviour of test specimens is presented in Tab. 9. Due to the crack propagation path, only E_{agg} and ν_{agg} should be considered. The reason is that, due to the non-existence of crack propagation through the aggregate (except for the first specimen with a marble inclusion), the fracture properties of the rock (such as $K_{Ic,agg}$, $G_{Ic,agg}$, etc.) should not affect the fracture behaviour of specimens.

	E_{agg}	ν_{agg}	$K_{Ic,\,agg}$	$G_{Ic,agg}$	$G_{F,agg}$
F_{max}	**–0.82**	0.48	**–0.93**	**–0.90**	**–0.90**
E	**–0.97**	0.10	**–0.84**	–0.69	–0.79
G_F	–0.32	0.78	–0.64	–0.77	–0.68
$K_{I,c}$	**–0.82**	0.47	**–0.93**	**–0.89**	**–0.89**
$K_{I,ce}$	–0.40	0.64	–0.66	–0.75	–0.67

Table 9: Influence of the mechanical fracture properties of rock on the overall fracture behaviour of test specimens: coefficients of correlation.

Correlation of micromechanical parameters measured by nanoindentation with the overall fracture behaviour

The correlation of micromechanical parameters measured by nanoindentation with the overall fracture behaviour of test specimens is presented in Tab. 10. There are very strong to perfect positive correlations between E_{mic} and both F_{max} and K_{Ic}. Also, the correlation between H and E is very strong and positive. There is a change in the case of $J(t)$ and F_{max}, where the very strong negative correlation exists. The other correlations are moderate to strong.

	$E_{mic,20}$	$E_{mic,50}$	H	$J(t)$
F_{max}	**1.00**	**0.96**	0.78	**–0.98**
E	0.67	**0.84**	**0.96**	–0.75
G_F	**0.80**	0.58	0.36	–0.69
$K_{I,c}$	**1.00**	0.96	0.78	**–0.99**
$K_{I,ce}$	**0.86**	0.67	0.38	–0.77

Table 10: Correlation of micromechanical parameters measured by nanoindentation with the overall fracture behaviour.

CONCLUSION

The chemical composition of rocks is correlated with their mechanical fracture parameters. The most important in terms of influence are Fe_2O_3, MnO and MgO. The other elements are primarily moderately correlated. At the same time, chemical composition of the rock is always a reflection of the representation of the main rock-forming minerals. Fe and Mg oxides are contained mainly in olivine, pyroxene, amphibole, and biotite. These results thus correspond to reality – above mentioned minerals rich in Fe and Mg are typical for basic and ultrabasic rocks (basalt, amphibolite, gabbro, eclogite, peridotite, etc.), which usually have very high strengths. For example, basalt is commonly used as an aggregate for high-strength concretes. However, it should be noted that not only the chemical and thus mineralogical composition, but also the structure and texture of rock have an influence on mechanical fracture parameters.

The influence of the chemical composition of rock on micromechanical parameters shows mostly weak or moderate correlations, and thus it seems that it does not significantly affect the micromechanical parameters measured by nanoindentation, while the influence of the mechanical fracture properties of rock seems to be important. These results are remarkable and will push our future research in the direction of studying the processes of aggregate-matrix interface formation more deeply. Nevertheless, the properties of the ITZ will be influenced mainly by the mineralogy of the newly formed phases at the aggregate-matrix interface, which unfortunately was not monitored. These newly formed phases are the results of chemical and physical reactions between the minerals (e. g. plagioclase, quartz) and cement phases (alite, belite, etc.) of the rock. In order to describe the effect of the chemical composition of rocks on the mechanical properties

of the produced concrete, several indexes have been established, see e.g. [33]. Nevertheless, these indexes are only applicable for a few types of rocks or for ordinary concretes.
The influence of mechanical fracture properties of rock on the overall fracture behaviour of test specimens is primarily visible in the very strong negative correlation between the Young's modulus of specimen material E and the Young's modulus of rock E_{agg}. These results are in disagreement with the literature; see [34] or [35]. However, it is necessary to realize that this literature concerns ordinary concrete and not specimens with a single inclusion. The fracture behaviour of such a special specimen is strongly influenced by the mechanical fracture properties of the interface due to the limited crack propagation direction, while in the case of ordinary concrete there are a lot of interfaces placed randomly in the volume, so crack propagation is a complex problem.
The correlation of micromechanical parameters with the fracture behaviour of specimens is indisputable and shows a very strong to perfect correlation. In other words, the micromechanical parameters of the ITZ have a direct influence on the fracture behaviour of cement-based composites.

ACKNOWLEDGEMENTS

Financial support provided by the Czech Science Foundation (GACR) under project No. 19-09491S (MUFRAS) and by Brno University of Technology under project No. FAST-J-21-7497 is gratefully acknowledged. Support from GACR 21-11965S is also acknowledged by the Czech Technical University in Prague (J. Němeček, nanoindentation of ITZ).
The authors would also like to thank the many kind colleagues who lent a helping hand, especially Petr Daněk and Patrik Bayer from Brno University of Technology's Institute of Building Testing and Institute of Chemistry, respectively for providing support for the performance of fracture tests and for scanning electron microscopy micrographs. Our thanks also go out to Alexandr Martaus from the Institute of Environmental Technology at VSB–Technical University of Ostrava, who kindly performed an analysis of rock chemical composition using X-ray fluorescence spectroscopy. These experimental results were accomplished using the Large Research Infrastructure ENREGAT supported by the Ministry of Education, Youth and Sports of the Czech Republic under project No. LM2018098.

REFERENCES

[1] Karihaloo, B. L. (1995). Fracture mechanics and structural concrete. New York: Wiley. ISBN 0-582-21582-x.
[2] European Committee for Standardization (2004), Eurocode 2: Design of concrete structures – Part 1-1: General rules, EN 1992-1-1, European Committee for Standardization, Brussels.
[3] Zacharda, V., Němeček, J., Šimonová, H., Kucharczyková, B., Vyhlídal, M., Keršner, Z. (2018). Influence of interfacial transition zone on local and overall fracture response of cementitious composites. Key Engineering Materials. 784, pp. 97−102. DOI: 10.4028/www.scientific.net/KEM.784.97.
[4] Randl, N. (2013). Design recommendations for interface shear transfer in fib Model Code 2010. Structural Concrete. 14(3), pp. 230−241. DOI: 10.1002/suco.201300003.
[5] Fedération internationale du béton (2013). fib Model Code for Concrete Structures 2010, Ernst & Sohn, Berlin.
[6] Farran, J. (1956). Contribution mineralogique a l'etude de l'adherence entre les constituants hydrates des ciments et les materiaux enrobes. Revue des Matiriaux de Construction. 491, pp. 155–157.
[7] Scrivener, K. L., Crumbie, A. K., Laugesen, P. (2004). The interfacial transition zone (ITZ) between cement paste and aggregate in concrete. Interface Science. 12(4), pp. 411–421. DOI:10.1023/B:INTS.0000042339.92990.4c.
[8] Diamond, S., Huang, J. (1998). Interfacial transition zone: reality or myth? In: Proceedings of the RILEM Second International Conference on the Interfacial Transition Zone in Cementitious Composites. London, E & FN Spon, pp. 3–39.
[9] Starý, J., Sitenský, I., Mašek, D., Gabriel, Z., Hodková, T., Vaněček, M., Novák, J., Kavina, P., (2020). Mineral commodity summaries of the Czech Republic, 2020 edition, data to 2019. Prague: Czech Geological Survey.
[10] Bukovská, Z., Soejono, I., Vondrovic, L., Vavro, M., Souček, K., Buriánek, D., Dobeš, P., Švagera, O., Waclawik, P., Řihošek, J., Verner, K., Sláma, J., Vavro, L., Koníček, P., Staš, L., Pécskay, Z., Veselovský, F. (2019). Characterization and 3D visualization of underground research facility for deep geological repository experiments: A case study of underground research facility Bukov, Czech Republic. Engineering Geology. 259. DOI: 10.1016/j.enggeo.2019.105186.

[11] Slivka, V., Vavro, M. (1996). The significance of textural and structural properties of North-Moravian basaltoids for the manufacture of mineral fibres. Ceramics-Silikáty. 40(4), pp. 149−159.
[12] Malíková, L., Vavro, L., Vavro, M., Keršner, Z. (2019). Evaluation of fracture response of Silesian granite specimens via Effective Crack Model approach and finite element analysis. Procedia Structural Integrity. 23, pp. 487−492. DOI: 10.1016/j.prostr.2020.01.133.
[13] EN 1936 (2006), Natural stone test methods - Determination of real density and apparent density, and of total and open porosity, European Committee for Standardization, 10 p., (in Czech).
[14] EN 13755 (2001), Natural stone test methods - Determination of water absorption at atmospheric pressure, European Committee for Standardization, 9 p., (in Czech).
[15] International Society for Rock Mechanics Commission on Testing Methods (1978), Suggested methods for determining sound velocity, International Journal of Rock Mechanics and Mining Sciences & Geomechanics Abstracts, 15(2), 53–58.
[16] International Society for Rock Mechanics Commission on Testing Methods (1979), Suggested methods for determining the uniaxial compressive strength and deformability of rock materials, International Journal of Rock Mechanics and Mining Sciences & Geomechanics Abstracts, 16(2), 137–140.
[17] International Society for Rock Mechanics Commission on Testing Methods (1988), Suggested methods for determining the fracture toughness of rock, International Journal of Rock Mechanics and Mining Sciences & Geomechanics Abstracts, 25(2), 71–96.
[18] Vavro, L., Souček, K. (2013). Study of the effect of moisture content and bending rate on the fracture toughness of rocks. Acta Geodynamica et Geomaterialia. 10(2), pp. 247−253. DOI:10.13168/AGG.2013.0025.
[19] Vavro, L., Malíková, L., Frantík, P., Kubeš, P., Keršner, Z., Vavro, M. (2019). An advanced assessment of mechanical fracture parameters of sandstones depending on the internal rock texture features. Acta Geodynamica et Geomaterialia. 16(2), pp. 157−168. DOI: 10.13168/AGG.2019.0013.
[20] Vyhlídal, M., Rozsypalová, I., Majda, T., Daněk, P., Šimonová, H., Kucharczyková, B., Keršner, Z. (2019). Fracture response of fine-grained cement-based composite specimens with special inclusions. Solid State Phenomena. 292, pp. 63–68. DOI: 10.4028/www.scientific.net/SSP.292.63.
[21] Goldstein, J., Newbury, D. E., Michael, J. R., Ritchie, N. W. M., Scott, J. H. J., Joy, D. C. (2018). Scanning electron microscopy and X-ray microanalysis. Fourth edition. New York: Springer. DOI: 10.1007/978-1-4939-6676-9.
[22] Němeček, J., Králík, V., Vondřejc, J. (2013). Micromechanical analysis of heterogeneous structural materials, Cement and Concrete Composite. 36 (1), pp. 85−92. DOI: 10.1016/j.cemconcomp.2012.06.015.
[23] Oliver, W., Pharr, G. (1992). An improved technique for determining hardness and elastic-modulus using load and displacement sensing indentation experiments. Journal of Materials Research. 7(6), pp. 1564−1583. DOI: 10.1557/JMR.1992.1564.
[24] Vyhlídal, M.; Klusák, J. (2020). A Crack Approaching the Edge of the Aggregate. Transactions of the VŠB – Technical University of Ostrava, Civil Engineering Series, 20 (2), pp. 47−52. DOI: 10.35181/tces-2020-0017.
[25] RILEM TC-50 FMC (1985). Determination of the fracture energy of mortar and concrete by means of three-point bend tests on notched beams. Materials and Structures. 18(106), pp. 287–290. DOI: 10.1007/BF02472918.
[26] Bourdette, B., Ringot, E., Ollivier, J. P. (1995). Modelling of the transition zone porosity. Cement and Concrete Research. 25(4), pp. 741−751.
[27] Scrivener, K. L., Crumbie, A. K., Pratt, P. L. (1987). A study of the interfacial region between cement paste and aggregate in concrete. MRS Proceedings. 114. DOI:10.1557/PROC-114-87.
[28] Asuero, A. G., Sayago, A., González, A. G. (2007). The Correlation Coefficient: An Overview. Critical Reviews in Analytical Chemistry. 36(1), pp. 41–59. DOI:10.1080/10408340500526766
[29] Kozak, M. (2009). What is strong correlation? Teaching Statistics. 31(3), pp. 85−86. DOI: 10.1111/j.1467-9639.2009.00387.x.
[30] Akoglu, H. (2018) User's guide to correlation coefficients, Turkish Journal of Emergency Medicine., 18(3), pp. 91-93. DOI: 10.1016/j.tjem.2018.08.001.
[31] Ratner, B. (2009). The correlation coefficient: Its values range between 1/−1, or do they? Journal of Targeting, Measurement and Analysis for Marketing. 17(2), pp.139−142. DOI:10.1057/jt.2009.5.
[32] Zhang, Z. X. (2002). An empirical relation between mode I fracture toughness and the tensile strength of rock. International Journal of Rock Mechanics and Mining Sciences. 39(3), pp. 401−406. DOI: 10.1016/S1365-1609(02)00032-1.

[33] Lampropoulou, P., Petrounias, P., Giannakopoulou, P., Rogkala, A., Koukouzas, N., Tsikouras, B., Hatzipanagiotou, K. (2020). The effect of chemical composition of ultramafic and mafic aggregates on their physicomechanical properties as well as on the produced concrete strength. Minerals, 10, 406, pp. 1−27. DOI: 10.3390/min10050406.
[34] Aïtcin, P.-C. (1998). High performance concrete. New York: E & FN Spon.
[35] Neville, A. M. (2011). Properties of concrete. 5th ed. New York: Pearson.